CHAPTER SEVEN
ESDM EVALUATION: EXPERIMENTAL RESULTS AND DISCUSSION

The experimental procedure yielded LDV and accelerometer data. This data was then processed and experimental results subsequently obtained. Specifically, velocity magnitude and phase along three orthogonal directions at a single frequency were obtained from the LDV data via ESDM and from the accelerometer data. The velocity results obtained from the accelerometer data served as a standard against which ESDM results were compared and ESDM ultimately evaluated. This chapter initially explains how ESDM and accelerometer results were obtained and presents these results; thereafter, the results are compared and briefly discussed.

Nomenclature

a	acceleration
f	frequency
Y	mobility
N	element interpolating function
v	velocity
v_x	velocity component in x-direction
v_y	velocity component in y-direction
v_z	velocity component in z-direction
x, y	spatial structure coordinate system Cartesian coordinates; spatial structure coordinate system Cartesian components
z	spatial structure coordinate system Cartesian component
1, 2, 3, 4	node labels
ξ	parametric element coordinate
η	parametric element coordinate
π	pi, 3.141…
ϕ	velocity phase angle
ϕ_x	relative phase angle associated with velocity in x-direction
ϕ_y	relative phase angle associated with velocity in y-direction
ϕ_z	relative phase angle associated with velocity in z-direction

μ_a uncertainty associated with accelerometers

μ_v uncertainty associated with velocity magnitude results obtained from accelerometer data

ESDM Results

Final ESDM results were derived from the LDV time-series data. First, once the time-series data from the LDV was collected and stored, another program contained within the ESDM software suite [62] reconstructed the time-series data. This program was controlled by an input file that specified 1) sensitivities for the LDV and force transducer data so that the final velocity results possessed the correct units, 2) the finite element mesh which modeled the front surface geometry and 3) statistical parameters[28] which controlled solution accuracy. The reconstructed time-series data was ultimately placed in a data file. Second, two final ESDM programs [64,65] generated the specified finite element mesh, processed the reconstructed time-series data and calculated the nodal velocity components for each finite element contained within the mesh. The finite element mesh created by ESDM is illustrated by Fig. 60[29]; the mesh contains seventy-two linear, quadrilateral finite elements. Third, the final nodal velocity solutions were written to a data file. Fourth, the tri-axial accelerometer locations within the finite element mesh were determined. Specifically, the six mounting block locations were determined within the mesh. Fifth, the parametric coordinates of the mounting block location within each element were calculated. Equation (150) describes a particular location within a linear, quadrilateral finite element [67]:

[28] Data collected at a particular scan point was deemed invalid if the correlation coefficient between the velocity and force signals was less than 0.9 and the *p*-value [63] was greater than 0.01.

[29] Figure 60 was originally created by display software included with the ESDM software suite [66].

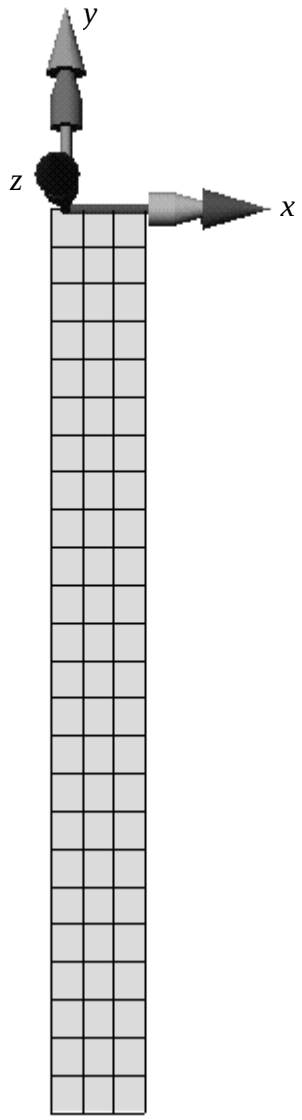

Figure 60. Finite element mesh created by ESDM which modeled the column front surface geometry

$$\begin{aligned} x &= N_1 x_1 + N_2 x_2 + N_3 x_3 + N_4 x_4 \\ y &= N_1 y_1 + N_2 y_2 + N_3 y_3 + N_4 y_4 \end{aligned}, \tag{150}$$

where the interpolating functions are polynomials of the form [68]:

$$
\begin{aligned}
N_1 &= \tfrac{1}{4}(1-\xi)(1-\eta) \\
N_2 &= \tfrac{1}{4}(1+\xi)(1-\eta) \\
N_3 &= \tfrac{1}{4}(1+\xi)(1+\eta) \\
N_4 &= \tfrac{1}{4}(1-\xi)(1+\eta)
\end{aligned}
\qquad (151)
$$

The only unknown terms in Eq. (150) were the parametric coordinates ξ and η. Unfortunately, Eq. (150) is non-linear with respect to the parametric coordinates; however, this was not a problem since MATLAB® contains a function that solves non-linear functions. Therefore, via Eq. (150) and MATLAB®, the parametric coordinates of the mounting block locations, or alternatively the accelerometer locations, within the finite element mesh were determined. Sixth, the three orthogonal velocity components at each accelerometer location were calculated. Like Eq. (150), Eq. (152) describes the velocity at a particular location within a linear, quadrilateral finite element:

$$
\begin{aligned}
v_x &= N_1 v_{x_1} + N_2 v_{x_2} + N_3 v_{x_3} + N_4 v_{x_4} \\
v_y &= N_1 v_{y_1} + N_2 v_{y_2} + N_3 v_{y_3} + N_4 v_{y_4} \\
v_z &= N_1 v_{z_1} + N_2 v_{z_2} + N_3 v_{z_3} + N_4 v_{z_4}
\end{aligned}
\qquad (152)
$$

The final two ESDM programs provided nodal velocities and the interpolating functions were known since the parametric coordinates were also known; therefore, the only unknown terms in Eq. (152) were the velocity components v_x, v_y and v_z. Again, MATLAB® evaluated Eq. (152) at each accelerometer location depicted by Fig. 61; the results are listed in Table 9. The velocity magnitudes listed in Table 9 are not relative to the applied excitation force; however, the phases listed are relative to the applied excitation force. Since, at present, the uncertainties associated with ESDM results cannot be calculated, no ESDM result uncertainties are specified.

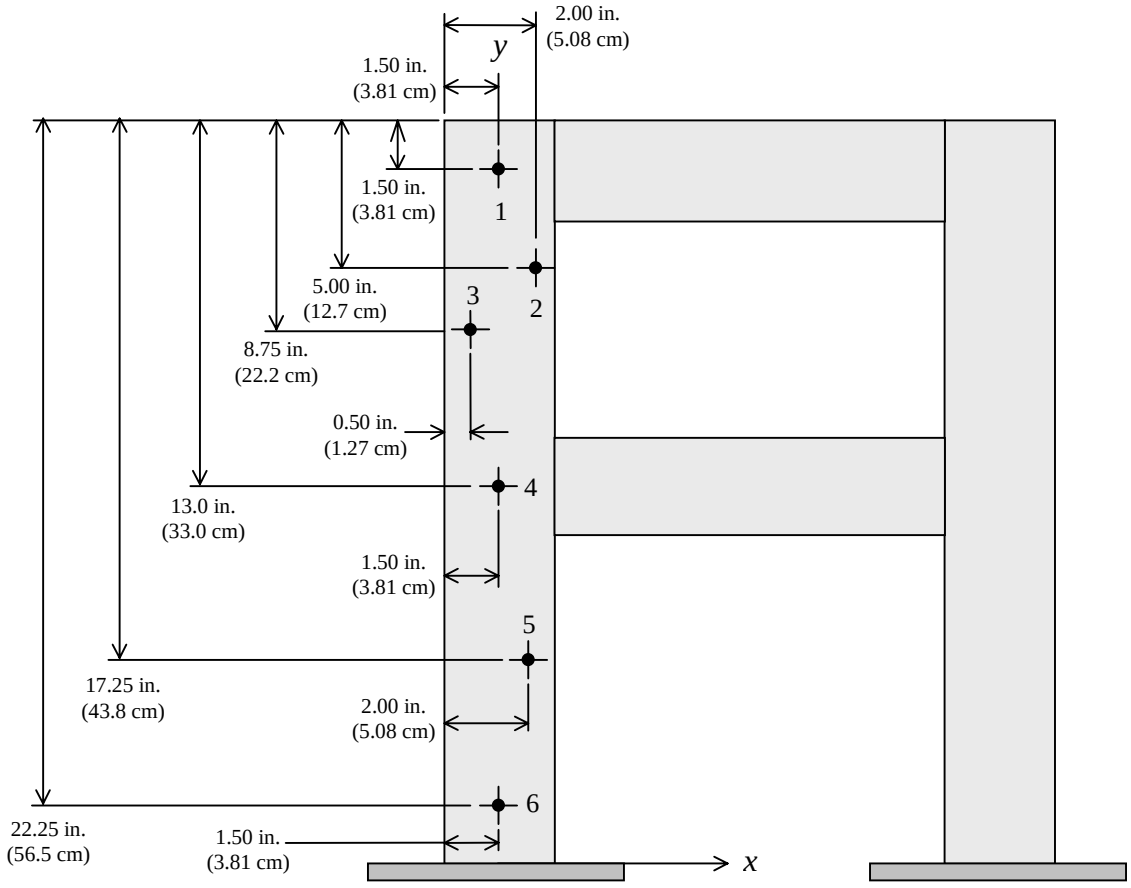

Figure 61. Tri-axial accelerometer configuration locations

Table 9. Velocity magnitude and relative phase results obtained via ESDM at the indicated accelerometer locations

Position	Horizontal In-Plane Velocity, v_x		Vertical In-Plane Velocity, v_y		Out-of-Plane Velocity, v_z	
	Magnitude $in \cdot s^{-1}$ ($mm \cdot s^{-1}$)	Phase °	Magnitude $in \cdot s^{-1}$ ($mm \cdot s^{-1}$)	Phase °	Magnitude $in \cdot s^{-1}$ ($mm \cdot s^{-1}$)	Phase °
1	0.0370 (0.939)	-96.4	3.90×10^{-3} (0.0990)	80.4	3.98×10^{-3} (0.101)	-86.3
2	0.0330 (0.837)	-96.8	3.09×10^{-3} (0.0786)	85.5	3.16×10^{-3} (0.0802)	-85.3
3	0.0297 (0.755)	-96.9	1.01×10^{-3} (0.0256)	99.9	3.59×10^{-3} (0.0914)	-86.4
4	0.0203 (0.516)	-97.5	1.35×10^{-3} (0.0342)	89.9	3.62×10^{-3} (0.0920)	-89.5
5	0.0133 (0.338)	-98.2	1.05×10^{-3} (0.0266)	72.9	2.06×10^{-3} (0.0523)	-90.5
6	5.12×10^{-3} (0.130)	-99.6	6.42×10^{-4} (0.0163)	92.9	1.48×10^{-3} (0.0377)	-100

The relative phases listed in Table 9 were not calculated directly from Eq. (152); rather, phase lag induced by the LDV filters was added to the results obtained from Eq. (152). During the experimental procedure, the LDV filters were set at a 1000 Hz break-frequency. This filter setting unfortunately induced an approximate 27° phase lag [69] into the LDV velocity data[30]. Thus, 27° was added to the relative phase values calculated via Eq. (152) to obtain the final relative phase results listed in Table 9.

A convergence test was conducted to determine whether the original finite element mesh, shown in Fig. 60, contained enough elements to adequately model the reconstructed velocity field. To test convergence, the results listed in Table 9 were compared with results obtained from another, denser finite element mesh at the same accelerometer locations. The original mesh was three elements wide and twenty-four elements high, contained seventy-two elements and possessed a mesh density of about one element per square inch (6 cm^2). The denser mesh was four elements wide and thirty-two elements high, contained 200 elements and possessed a mesh density of about two elements per square inch (6 cm^2). Percent differences between velocity component magnitudes obtained from each mesh at the same accelerometer locations averaged only about 1%. Furthermore, absolute differences between relative phase components were negligible. Therefore, since the results obtained from each mesh do not significantly differ, the original finite element mesh adequately modeled the reconstructed velocity field.

[30] The LDV filters induced no magnitude attenuation [70].

Accelerometer Results

Velocity results were easily obtained from the accelerometer data. Acceleration linear spectrum and mobility data were collected recorded by the signal analyzer. The linear spectrum acceleration data yielded velocity magnitude according to the following equation:

$$v = \frac{a}{2\pi f}, \tag{154}$$

where

$$f = 144 \text{ Hz}. \tag{155}$$

The mobility data yielded velocity phase according to the following equation:

$$\phi = \tan^{-1}\left[\frac{\text{Im}(Y)}{\text{Re}(Y)}\right]. \tag{156}$$

Table 10 lists velocity results obtained from the accelerometer data at the accelerometer locations depicted by Fig. 61. Again, the velocity magnitudes listed are not relative to the excitation force; however, the phases listed are relative to the excitation force. The uncertainty associated with accelerometers is [71]

$$\mu_a = 3.86 \ \frac{\text{in}}{\text{s}^2} \ \left(98.1 \ \frac{\text{mm}}{\text{s}^2}\right); \tag{157}$$

therefore, the uncertainty associated with velocity magnitudes in Table 10 is

$$\mu_v = \frac{\mu_a}{2\pi f} = 4.27\text{x}10^{-3} \ \frac{\text{in}}{\text{s}} \ \left(0.108 \ \frac{\text{mm}}{\text{s}}\right), \tag{158}$$

where again

$$f = 144 \text{ Hz}. \tag{160}$$

Such uncertainty exceeds all the velocity magnitudes in the *y*-direction and most of the velocity magnitudes in the z-direction.

Table 10. Velocity magnitude and relative phase results obtained from accelerometer data collected at the indicated locations

Position	Horizontal In-Plane Velocity, v_x		Vertical In-Plane Velocity, v_y		Out-of-Plane Velocity, v_z	
	Magnitude $in \cdot s^{-1}$ ($mm \cdot s^{-1}$)	Phase °	Magnitude $in \cdot s^{-1}$ ($mm \cdot s^{-1}$)	Phase °	Magnitude $in \cdot s^{-1}$ ($mm \cdot s^{-1}$)	Phase °
1	0.0402 (1.00)	-95.9	1.95×10^{-3} (0.0335)	-91.1	4.37×10^{-3} (0.103)	-89.3
2	0.0341 (0.865)	-96.3	4.53×10^{-4} (0.0115)	130	2.80×10^{-3} (0.0712)	-84.7
3	0.0301 (0.764)	-96.9	1.22×10^{-3} (0.0309)	-110	3.52×10^{-3} (0.0893)	-92.6
4	0.0204 (0.517)	-97.5	3.48×10^{-4} (8.84×10^{-3})	-146	3.16×10^{-3} (0.0803)	-91.7
5	0.0122 (0.310)	-99.5	6.61×10^{-4} (0.0168)	106	7.13×10^{-4} (0.0181)	-86.2
6	4.53×10^{-3} (0.115)	-106	7.80×10^{-4} (0.0198)	109	2.15×10^{-4} (5.47×10^{-3})	-94.7

Result Comparison and Discussion

Figures 62 through 67 compare velocity results obtained from ESDM and the accelerometer data. Specifically, Figs. 62 and 63, respectively, compare horizontal in-plane (*x*-direction) velocity magnitude and relative phase results at each accelerometer location. Likewise, Figs. 64 and 65, respectively, compare vertical in-plane (*y*-direction) velocity magnitude and relative phase results and Figs. 66 and 67, respectively, compare out-of-plane (*z*-direction) velocity magnitude and relative phase results.

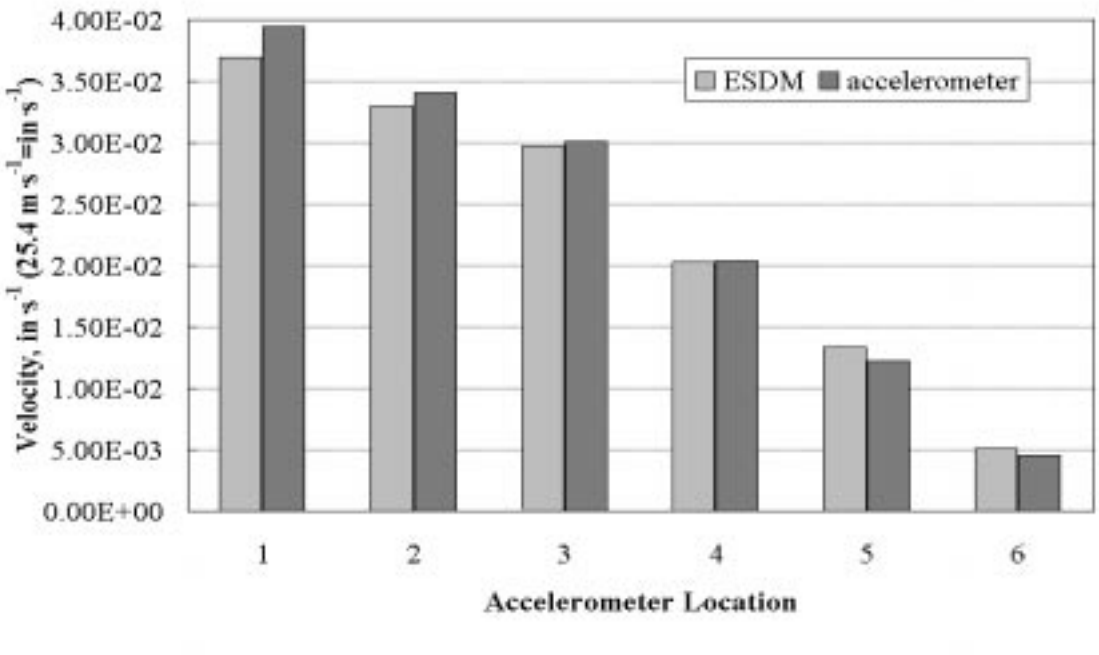

Figure 62. Velocity magnitude in *x*-direction obtained from ESDM and accelerometer data at each accelerometer location

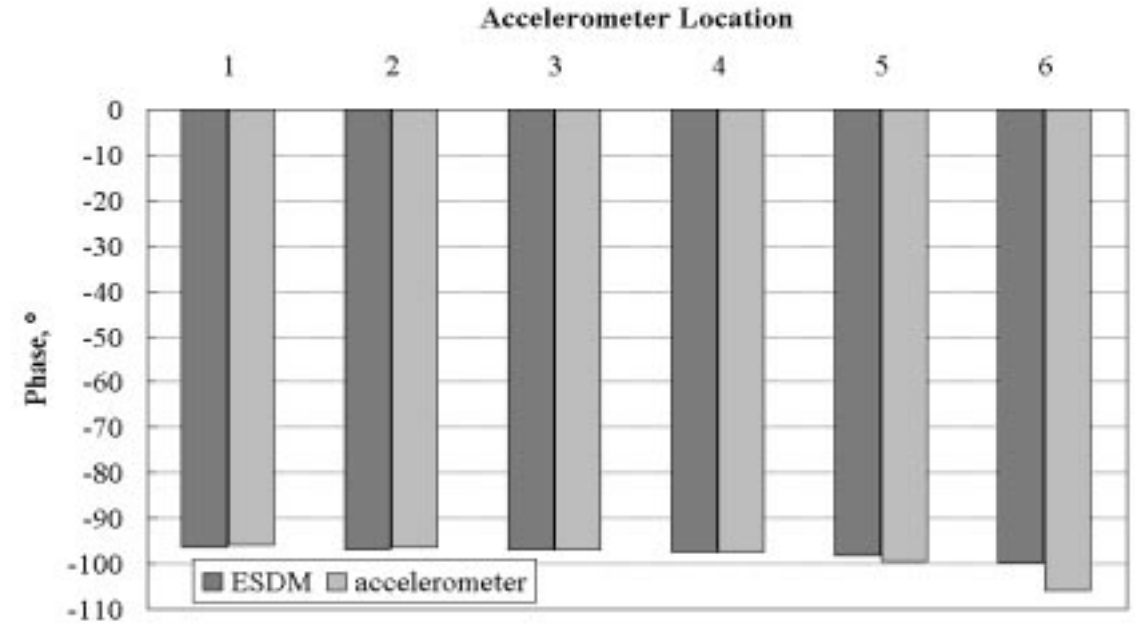

Figure 63. Relative phase in *x*-direction between velocity and excitation force obtained from ESDM and accelerometer data at each accelerometer location

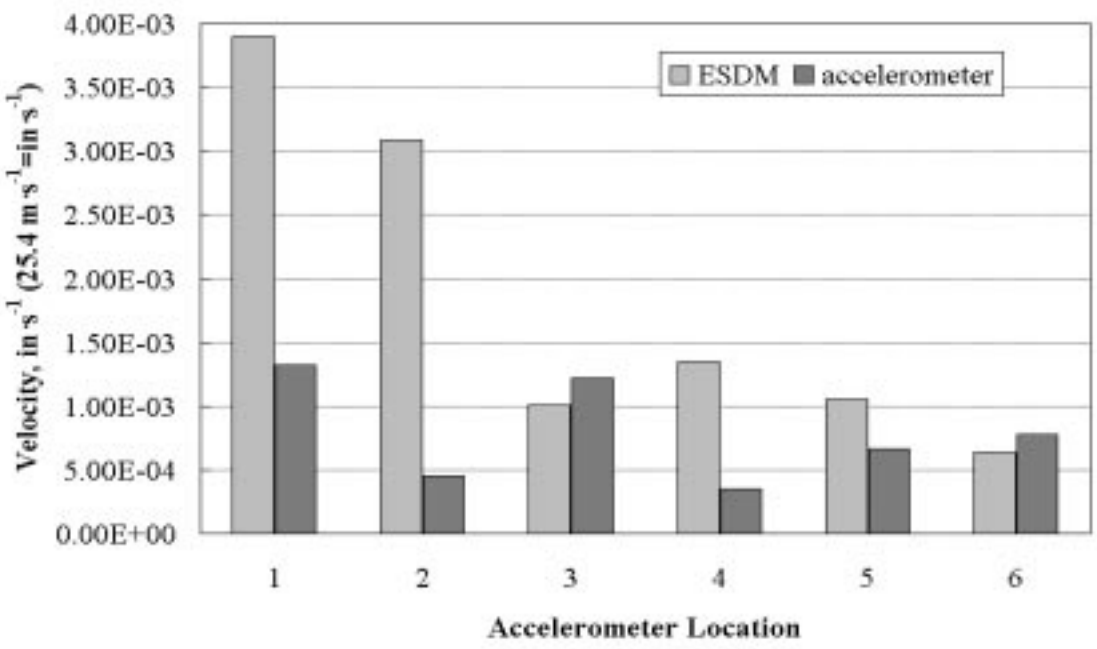

Figure 64. Velocity magnitude in *y*-direction obtained from ESDM and accelerometer data at each accelerometer location

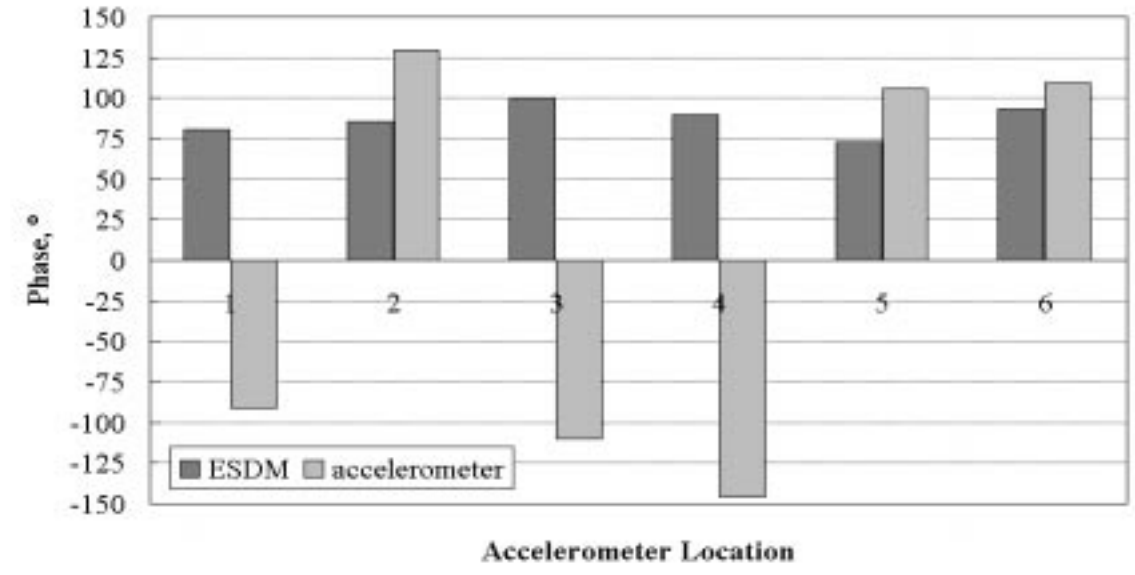

Figure 65. Relative phase in *y*-direction between velocity and excitation force obtained from ESDM and accelerometer data at each accelerometer location

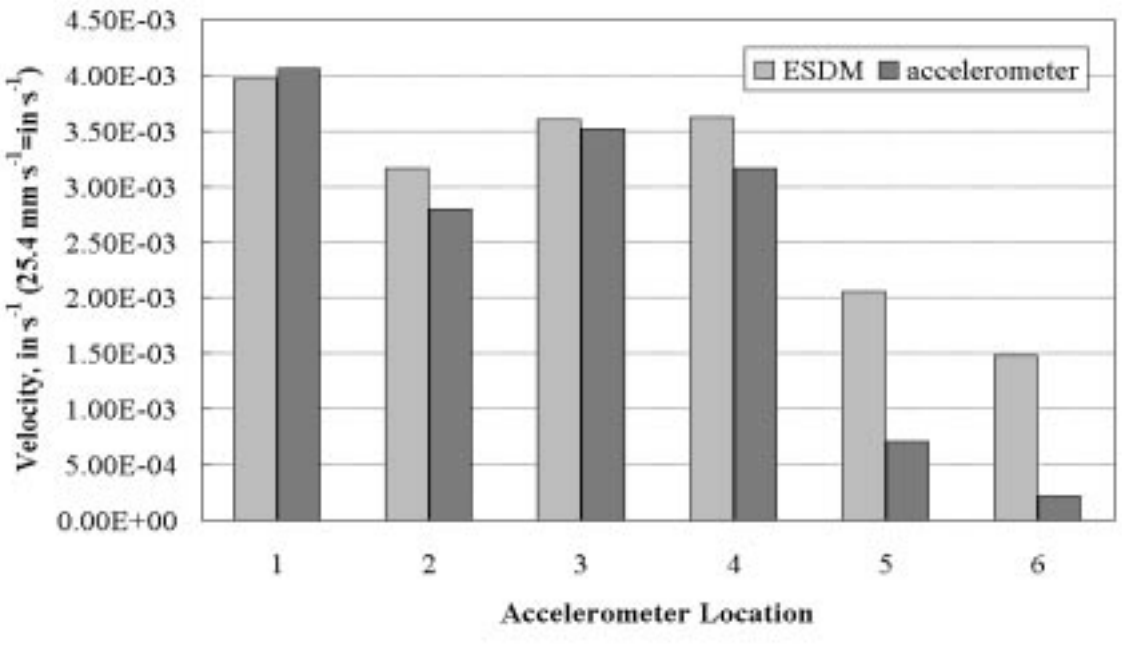

Figure 66. Velocity magnitude in *z*-direction obtained from ESDM and accelerometer data at each accelerometer location

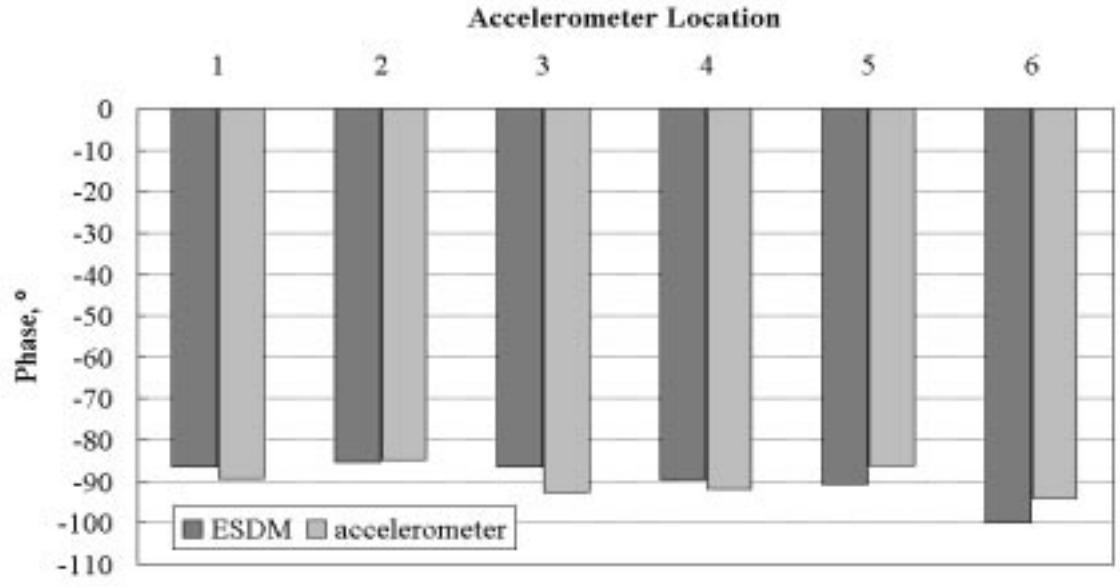

Figure 67. Relative phase in *z*-direction between velocity and excitation force obtained from ESDM and accelerometer data at each accelerometer location

Table 11 also compares ESDM and accelerometer velocity results. Specifically, Table 11 compares velocity magnitude and phase comparisons between like components at the six accelerometer locations. Magnitude comparisons among the velocity components are expressed as percent differences between ESDM and accelerometer results with the accelerometer results serving as the standard. Percent difference between velocity component magnitudes is

$$\Delta|v_i| = \left(\frac{|v_i|_{\text{ESDM}} - |v_i|_{\text{accelerometer}}}{|v_i|_{\text{accelerometer}}} \right) \cdot 100 , \tag{157}$$

where the subscript i represents either an x, y or z component and the vertical bars indicate velocity magnitude (modulus). Relative phase comparisons among the velocity components at each accelerometer location are expressed as simple differences between ESDM and accelerometer results with the accelerometer results serving as the standard. Relative phase difference is

$$\Delta\phi_i = \phi_i|_{\text{ESDM}} - \phi_i|_{\text{accelerometer}} , \tag{158}$$

Table 11. Magnitude and relative phase comparisons between velocity components obtained from ESDM and the accelerometer data at the six accelerometer locations

Location	**Horizontal In-Plane Velocity**		**Vertical In-Plane Velocity**		**Out-of-Plane Velocity**	
	$\Delta\lvert v_x\rvert$ **%**	$\Delta\phi_x$ **°**	$\Delta\lvert v_y\rvert$ **%**	$\Delta\phi_y$ **°**	$\Delta\lvert v_z\rvert$ **%**	$\Delta\phi_z$ **°**
1	6.10	0.5	196	171	1.94	3
2	3.24	0.5	583	44.5	12.6	0.6
3	1.18	0.0	17.2	210	2.35	6.2
4	1.94	0.0	287	236	14.6	2.2
5	9.03	1.3	58.3	33.1	189	4.3
6	13.0	6.4	17.7	16.1	589	5.3

where *i* again represents an *x*, *y* or *z* component.

Figures 62 and 63 and Table 11 clearly indicate that velocity magnitude and relative phase results in the *x*-direction obtained from ESDM at the six accelerometer locations closely match accelerometer results at the same locations. Only at the final two accelerometer locations near the bottom of the column front surface do the ESDM and accelerometer results slightly diverge. This is reasonable and not surprising since *x*-component velocities near the bottom of the column were extremely low. Such low velocities were near the noise floor for both the LDV and the accelerometers, approximately $2x10^{-4}$ in·s^{-1} ($3x10^{-3}$ mm·s^{-1}) for both transducers at nearby frequencies.

Likewise, Figs. 66 and 67 and Table 11 indicate that velocity magnitude and relative phase results in the *z*-direction obtained from ESDM at the first four accelerometer locations closely match accelerometer results at the same locations. However, agreement is not as close as for the *x*-direction. Worse overall agreement compared to the *x*-direction results was not unexpected since *z*-component velocities were much lower than *x*-component velocities. At the last two accelerometer locations, ESDM and accelerometer results vary greatly. Extremely low z-direction velocities near the bottom of the front column surface caused this phenomena. Again, such velocities were near the noise floor for each transducer.

Unlike the *x*- and *z*-directions, Figs. 64 and 65 and Table 11 indicate that velocity magnitude and relative phase results in the *y*-direction obtained from ESDM at all six accelerometer locations vary wildly relative to the same results obtained from the

accelerometers. Again, this is easily explained. No attempt was made to control *y*-direction motion and almost no vertical frame motion existed. Therefore, only extremely small vertical velocity components existed; whatever vertical velocities ESDM reconstructed and the accelerometers measured were essentially random noise. Consequently, the velocity results obtained from both ESDM and the accelerometers show great variations. However, an interesting phenomena is evident: the ESDM results are more consistent than the accelerometer results. Specifically, velocity magnitudes obtained via ESDM demonstrate a slight velocity gradient down the column and relative phase is maintained. Overall, especially considering relative phase, discontinuities were less evident than demonstrated by the accelerometer results. A possible explanation for this phenomena follows. The accelerometers measured acceleration at different points on the column front surface. That is, the accelerometers sampled the velocity field at discrete locations. From the acceleration data, velocity was obtained. Therefore, the velocity obtained from an accelerometer at a particular location did not depend on velocities at other locations. However, ESDM relies upon a finite element formulation that minimizes the least-squares error between LDV data and the modeled velocity field. Consequently, velocity obtained via ESDM at a particular location depended upon velocities at other locations. This dependency possibly limited extreme magnitude and relative phase discontinuities down the column front surface. Hence, the apparent consistency exhibited by ESDM results in the *y*-direction is reasonable.

Figures 68 and 69 show maximum velocity magnitudes obtained from ESDM across the entire front column surface. Specifically, Fig. 68 shows horizontal in-plane

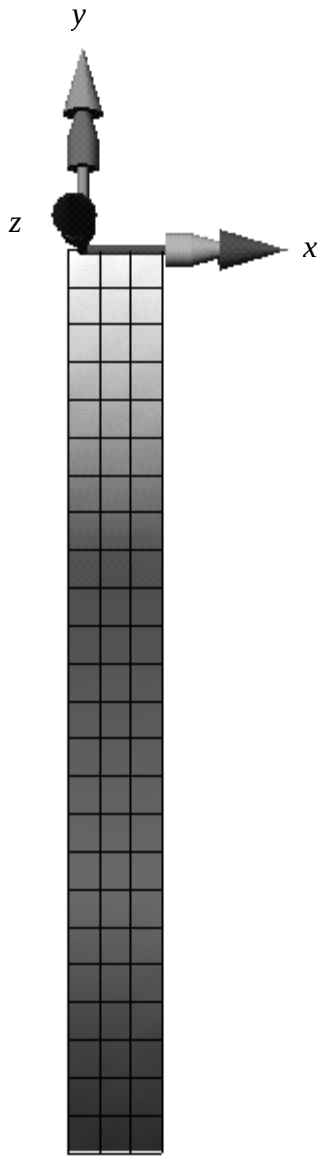

Figure 68. Horizontal in-plane ESDM velocity magnitude in *x*-direction

velocity magnitude in the *x*-direction; similarly, Fig. 69 shows out-of-plane velocity magnitude in the *z*-direction. ESDM visualization software created both figures. Velocity magnitudes range from approximately $5x10^{-3}$ in·s^{-1} (0.1 mm·s^{-1}) to $4x10^{-2}$ in·s^{-1} (1 mm·s^{-1}) in Fig. 68. In Fig. 69, velocity magnitudes range from about $5x10^{-4}$ in·s^{-1} ($1x10^{-2}$ mm·s^{-1}) to $4x10^{-3}$ in·s^{-1} (0.1 mm·s^{-1}). Velocity magnitudes are lowest within dark

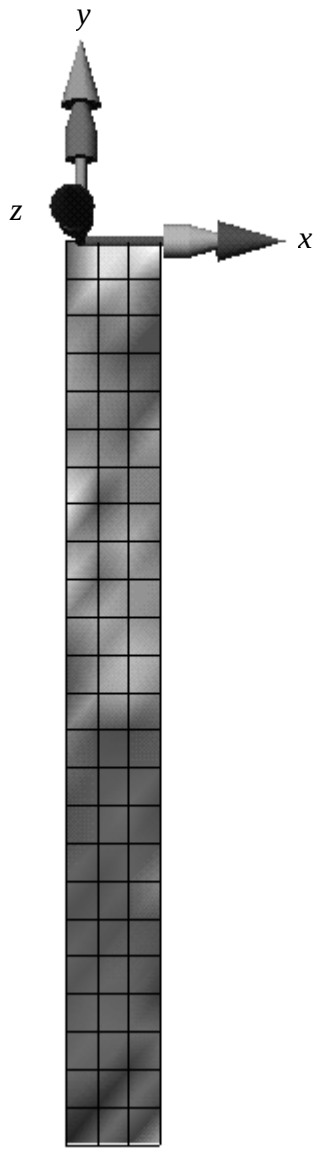

Figure 69. Out-of-plane ESDM velocity magnitude in *x*-direction

areas and highest within light areas. As expected, the in-plane results demonstrate a smooth, decreasing velocity gradient down the column face; however, the out-of-plane results do not demonstrate such a gradient. Moreover, as shown in Fig. 66, the out-of-plane velocity magnitudes obtained from the accelerometer data demonstrate the same phenomena. Therefore, the phenomena is most likely attributable to test structure

motion. Such motion was unexpected since the original test structure finite element model did not visually exhibit similar motion. Furthermore, such motion is not easily explained.